Ultra-high-Q resonances in plasmonic metasurfaces

M. Saad Bin-Alam[1,†], Orad Reshef[2,*,†], Yaryna Mamchur[3,1], M. Zahirul Alam[2], Graham Carlow[4], Jeremy Upham[2], Brian T. Sullivan[4], Jean-Michel Ménard[2], Mikko J. Huttunen[5], Robert W. Boyd[1,2,6], and Ksenia Dolgaleva[1,2]

[1]School of Electrical Engineering and Computer Science, University of Ottawa, Ottawa, ON K1N 6N5, Canada
[2]Department of Physics, University of Ottawa, 25 Templeton Street, Ottawa, ON K1N 6N5, Canada
[3]National Technical University of Ukraine "Igor Sikorsky Kyiv Polytechnic Institute," Kyiv, Ukraine
[4]Iridian Spectral Technologies Inc., 2700 Swansea Crescent, Ottawa, ON K1G 6R8, Canada
[5]Photonics Laboratory, Physics Unit, Tampere University, P.O. Box 692, FI-33014 Tampere, Finland
[6]Institute of Optics and Department of Physics and Astronomy, University of Rochester, Rochester, NY 14627, USA
[*]Corresponding author: orad@reshef.ca
[†]MSBA and OR contributed equally to this work.

Resonant cavities play a crucial role in many aspects of science and engineering[1,2]. A resonator with a large quality-factor (Q-factor) is essential to many applications in photonics, such as filtering[3], delay lines and memories[4], lasing[5,6], switching[7,8], spectroscopy[9], sensing[10–13], and nonlinear optical processes[14], among others[15–18]. Recently, the rapid development of nanofabrication technology has increased the appeal of nanostructured metasurfaces[19]. A metasurface with a large Q-factor could be used as a cavity for an ultra-flat nano-laser with a large transverse mode size[20,21], or to increase light-matter interactions[22–27] (*e.g.*, for THz-wave generation[28], entangled photon-pair generation[29], or deterministic single-photon sources[30]). However, to date, experimental demonstrations of metasurface nanoresonators have yet to produce Q-factors in excess of the order of 10^2, even for low-loss dielectric platforms[31–34]. In this Letter, we report the experimental observation of a metasurface nanoresonator with a Q-factor of 2400 in the telecommunication C band. This value is an order of magnitude higher than the previously reported values for any metasurface platform, and is enabled by surface lattice resonances aided by the proper choice of nanostructure dimension, large array sizes, and the use of a strongly collimated light source. Moreover, it was achieved with an array of plasmonic nanostructures, usually considered too lossy to support high Q-factor resonances due to high optical absorption in metals. Our results demonstrate that surface lattice resonances provide an exciting and unexplored method to achieve ultra-high-Q resonances in metasurfaces, and could pave the way to flexible wavelength-scale devices for any optical resonating application.

The core building blocks of plasmonic metasurfaces are metal nanostructures of sub-wavelength dimension[19,35]. These nanostructures exhibit localized surface plasmon resonances (LSPRs), where electromagnetic fields couple to the free-electron plasma of a conductor at a metal-dielectric interface[36,37]. An incident light beam induces a material polarization within the nanostructure, scattering light according to the moment of the nanoparticle. Thus, depending on its shape, an individual nanoparticle may act as a lossy dipole antenna[38] with many applications ranging from nanolasing to nonlinear optics[19,39,40]. However, these LSPRs typically exhibit low Q-factors (*e.g.*, $Q < 10$) due to the intrinsic absorption loss of metals. As the Q-factor is related to the light-matter interaction time as well as to enhancements to the electric field, it is typically desirable to maximize this quantity[18]. Low Q-factors therefore hinder the potential applications of plasmonics-based metasurface devices, and alternative methods of obtaining large Q-factor resonances in a metasurface have long been sought after.

In recent years, plasmonic metasurfaces supporting resonances arising from *periodically* arranged nanostructures have been a topic of intense study[32,41–48]. Such resonances are called surface lattice resonances (SLRs). Here, the individual responses from the surface plasmons of many individual nanostructures couple to in-plane diffraction orders of the periodic array to form a collective response[41,42]. As a consequence, a relatively high-Q resonance can emerge at an optical wavelength $\lambda_{\mathrm{SLR}} \approx nP$, close to the product of the

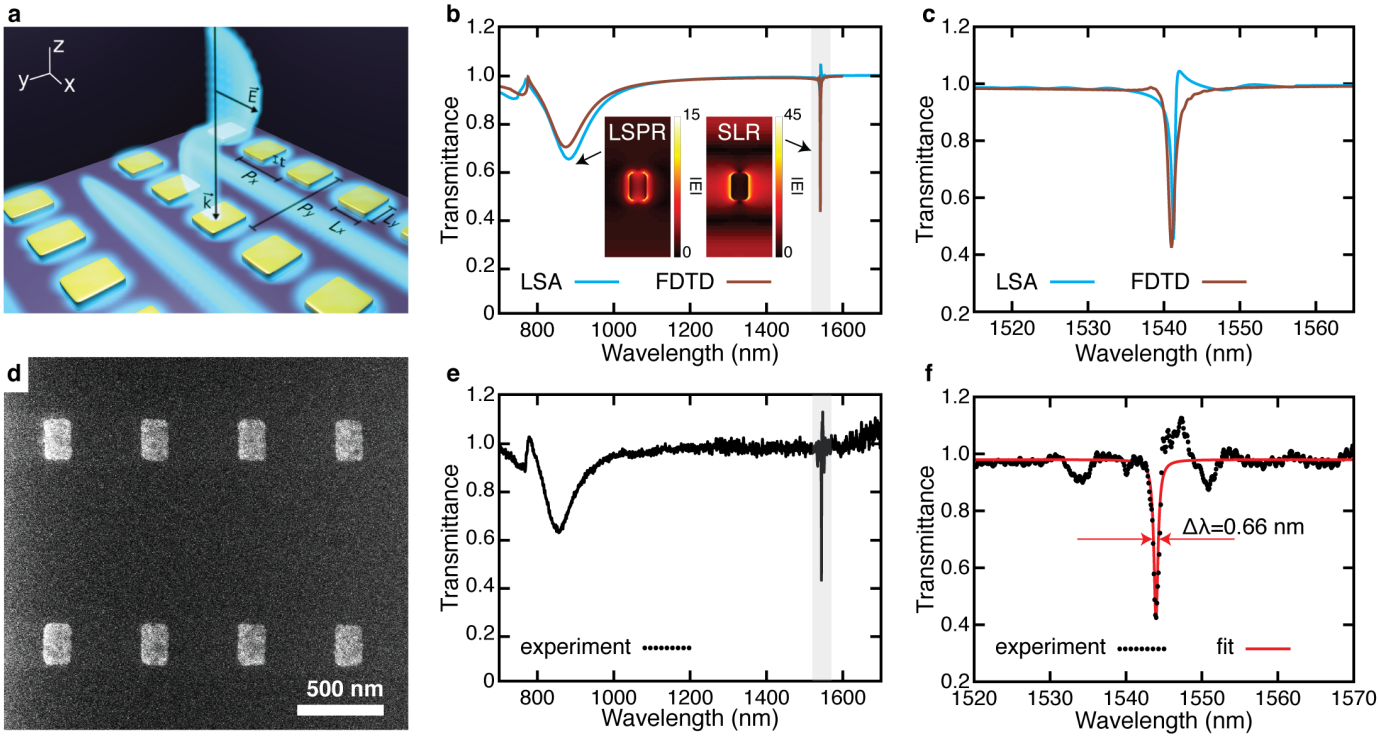

Fig. 1 | High-Q metasurface nanocavities using arrays of plasmonic nanostructures. a, Schematic of the metasurface consisting of a rectangular array of rectangular gold nanostructures. Here, $L_x = 130$ nm, $L_y = 200$ nm, $t = 20$ nm, $P_x = 500$ nm, and $P_y = 1060$ nm. **b,** Numerical (FDTD) and semi-analytic (LSA) calculations of the transmission spectrum of this metasurface for x-polarized light. Both the LSPR and the SLR are observed in these results. **Inset,** The simulated magnitude of the electric field $|E|$ for the entire unit cell of both LSPR and SLR modes. The colorbar indicates the relative magnitude when normalized to the incident plane wave. **c,** Zoomed plot of the highlighted region in **(b)**, exhibiting the narrow linewidth SLR ($Q \sim 3000$). **d,** Helium ion microscope image of the fabricated metasurface prior to cladding deposition. **e,** Measured transmission spectrum. **f,** Zoomed plot of the highlighted region in **(e)**. The red line is a Lorentzian fit, yielding a linewidth of $\Delta\lambda = 0.66$ nm, corresponding to $Q = 2400$.

refractive index of the background medium n and the lattice period P[45,49,50]. Recent theoretical studies of this platform have even predicted Q-factors on the order of 10^3 by properly engineering the dimensions of the individual nanostructures and the period of the lattice[43,44,47,48]. However, to date, the highest experimentally observed Q-factor in an SLR-based metasurface is 320[34]. The disparity between theory and experiment has so far been attributed to fabrication imperfections[42–44], or to the addition of an adhesion layer[34].

Inspired by this discrepancy, we have performed a detailed investigation to determine the three mitigating factors that most drastically affect the observed Q of an SLR-based metasurface: the nanostructure geometry, the array size, and the spatial coherence of the light source. Using the results of this study, we demonstrate a plasmonic metasurface capable of supporting high-Q SLRs. The metasurface in consideration consists of a rectangular array of rectangular gold nanostructures embedded in a homogeneous glass environment (Fig. 1a). The overcladding is carefully matched to the substrate material to ensure a symmetric cladding index, as it has been shown that the Q of an SLR may be affected by the homogeneity of the environment[41,51]. As shown by the numerical predictions in Figs. 1b – c, for an x-polarized beam, this metasurface is expected to support an LSPR at $\lambda_{\mathrm{LSPR}} = 830$ nm and an SLR around $\lambda_{\mathrm{SLR}} = 1550$ nm. The SLR linewidth is substantially narrower than that of the LSPR, corresponding to a much higher Q-factor. Incidentally, the inset field profiles in Fig. 1b also reveal that the SLR provides a more significant field enhancement, with $|E_{\max}(\lambda_{\mathrm{SLR}})| \sim 3|E_{\max}(\lambda_{\mathrm{LSPR}})|$. Figure 1d shows an image of the fabricated device with dimensions matching those of the simulations. The measured transmission spectra are presented in Figs. 1e – f, closely matching the predicted spectrum. Notably, the full width at half-maximum of the linewidth is only $\Delta\lambda = 0.66$ nm, corresponding to a record-high quality factor of $Q = 2400$. This value is in very close agreement with semi-analytic calculations performed

using the Lattice Sum approach, where $Q \sim 3000$ (see Methods for details). In order to observe this value for the Q-factor, both the metasurface and the measurement apparatus needed to be arranged with a few considerations in mind which we describe in greater detail below.

First, the individual structures need to be engineered to exhibit the appropriate response at λ_{SLR}. The optical response of a nanostructure can be described using the polarizability of a Lorentzian dipole,

$$\alpha(\omega) = \frac{A_0}{\omega - \omega_0 + i\gamma}, \tag{1}$$

where A_0 is proportional to the oscillator strength, $\omega_0 = 2\pi c/\lambda_{LSPR}$ corresponds to the nanoparticle resonance frequency, and γ is the damping term. These quantities all depend on the particle geometry (here, the length L_y and width L_x of a rectangular bar). The contribution of the particle lattice to the polarizability can be introduced using the lattice-sum approach[50–52]:

$$\alpha^*(\omega) = \frac{\alpha(\omega)}{1 - \varepsilon_0 \alpha(\omega) S(\omega)}, \tag{2}$$

where $\alpha^*(\omega)$ is known as the effective polarizability of the entire metasurface, and $S(\omega)$ corresponds to the lattice sum. This latter term depends only on the arrangement of the lattice. An SLR appears approximately where $S(\omega)$ exhibits a pole, at $\omega_{SLR} = (2\pi c/\lambda_{SLR})$. At this spectral location, the individual responses of all of the nanostructures contribute cooperatively[52].

Equation (2) may be used to predict the optical response of the entire metasurface, including the behaviour of its many resonances, as a function of the geometry of its nanostructures (see Methods): changing the geometry of the nanostructures[53] acts to change their individual resonance wavelengths λ_{LSPR}, oscillator strengths A_0, and damping constants γ. In turn, adjusting these values changes the polarizability of the nanostructures throughout the spectrum, including at the surface lattice resonance wavelength $\alpha(\omega_{SLR})$, and therefore the response of the entire metasurface $\alpha^*(\omega_{SLR})$. By contrast, the spectral location of the SLR wavelength is dictated mainly by the lattice period and the background index $\lambda_{SLR} \approx nP$[45,49,50]. In other

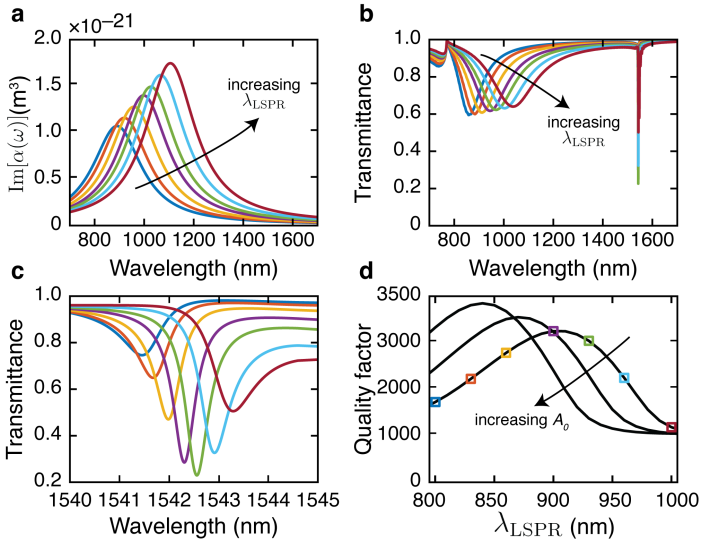

Fig. 2 | Coupling to a surface lattice resonance. The colors in parts **(a)** through **(d)** are consistent, corresponding to the same type of nanoparticle. **a,** The imaginary part of the individual particle polarizability for various nanostructures with increasing resonance wavelength λ_{LSPR}, holding both the oscillator strength A_0 and the damping term γ fixed. **b,** Simulated broadband transmission spectra for gold nanostructure arrays as a function of tuning λ_{LSPR}. By tuning the LSPR wavelength, the extinction factor of the SLR is observed to change near $\lambda = 1542$ nm. While λ_{LSPR} changes dramatically, the SLR wavelength λ_{SLR} does not change much. **c,** Zoomed in plot of the SLR in **(b)**. **d,** The Q-factor of the surface lattice resonance as a function of λ_{LSPR} for various oscillator strengths A_0. The optimal LSPR wavelength for a high-Q SLR changes as a function of A_0. The squares indicate the Q values extracted from the curves in **(c)**.

words, the lattice geometry governs the presence of the SLR, and the nanostructure geometry dictates its coupling efficiency to free space. Indeed, some recent theoretical studies in this platform have predicted Q-factors on the order of 10^3 by properly selecting the dimensions of the individual nanostructures[43,44,47,48].

We reproduce this dependence in this platform explicitly by plotting the calculated transmission of a metasurface (see Methods) as a function of nanostructure geometry (Fig. 2). (The dependence of the SLR behaviour on particle dimensions is also demonstrated using full-wave simulations in Sec. S1: Dependence of SLR behaviour on particle dimensions.) Here, we hold the oscillator strength A_0 and damping term γ constant and slowly increase the nanoparticle resonance wavelength λ_{LSPR}. In Figs. 2b – c, the SLR wavelength does not change substantially from its location around $\lambda_{\mathrm{SLR}} = 1542$ nm; however, the extinction ratio ΔT and the linewidth $\Delta\lambda$ of the resonance change dramatically. In Fig. 2d, we plot the extracted Q-factors for these SLRs, and for other values of A_0, as well (see Sec. S2: Q-factor extraction for the fits). We find that for every given value of A_0, there is a corresponding λ_{LSPR} for which light couples optimally to the lattice resonance at λ_{SLR} and produces the highest Q-factor. The optimal conditions are therefore found in the balance between increasing α relative to P_y (*i.e.,* increasing coupling strength), and maintaining a large spectral gap between λ_{LSPR} and λ_{SLR} (*i.e.,* limiting Ohmic losses associated with metallic nanoparticles). The trade-off between coupling and loss is a traditional one for optical resonators and is reproduced in this platform[54].

Next, we study the dependence of the Q-factor on the array size. For certain metasurfaces, it has already been shown that larger array sizes lead to better device performance[31,55,56]. Indeed, a few theoretical works have suggested that increasing the array size of a metasurface could be the dominant factor for increasing the Q-factor of an SLR[43,55]. This dependence makes some intuitive sense — since high-Q operation requires low absorption losses, we are required to operate the device far from the LSPR. However, at a sufficiently far operating wavelength, the scattering cross-section is also small, resulting in each antenna scattering very weakly. Consequently, far from the LSPR, one requires a sufficiently large number of scatterers to build up the resonance. Equivalently, the standing wave mode in an SLR consists of counter-propagating surface waves; therefore, a larger array provides an expanded propagation length in the cavity to support these modes.

To examine the dependence of Q on the number of nanostructures explicitly, we fabricated and characterized a series of devices of increasing array size Figure 3 shows the resulting transmission spectra, as well as their corresponding semi-analytic predictions. The observed Q-factors increase monotonically as a function of array size (Fig. 3b – see Sec. S2: Q-factor extraction for the fits). In the smallest array (300×300 μm^2), the SLR is almost imperceptible. This trend might help explain the relatively low Q values observed in previous studies[19,42,43,55] where array sizes were typically no larger than 250×250 μm^2, likely due to the relatively slow write-speed of the e-beam lithography process necessary for fabrication[34,41,48]. By contrast, our devices have array sizes reaching up to 600×600 μm^2 (see Sec. S3: Image of the device).

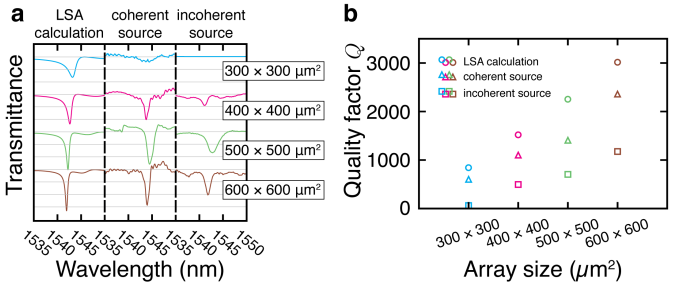

Fig. 3 | Effects of array size and spatial coherence of light source. a, Calculated and measured (using coherent and incoherent sources) transmission spectra for identical metasurface arrays of varying size (from top to bottom: 300×300, 400×400, 500×500, and 600×600 μm^2, respectively). The spectra are offset for clarity, and each vertical division corresponds to an increment of $\Delta T = 0.2$ in transmittance. **b,** The Q-factors extracted from Lorentzian fits to the calculations and to the measurements shown in **(a)**. An increase in the number of nanostructures in the array results in an increase in the estimated Q-factors. Additionally, the observed Q-factor is globally larger for each array when measured using the coherent source.

Finally, it is of critical importance to consider all aspects of the characterization system in order to get an accurate measurement of the Q-factor. In particular, we have found that the spatial coherence of the probe beam was critical to obtaining a clean measurement of the dip in transmission indicating a resonance. A

spatially coherent beam, such as a laser, will excite every region of the metasurface in phase, producing a clearer resonance. Furthermore, in our particular experiment, the transmitted signal from our coherent supercontinuum source was brighter and could be collimated more tightly than our incoherent thermal source. Therefore, the light collected from the metasurface array could be isolated with a smaller pinhole in the image plane, selecting the signal coming from nanostructures at the centre of the array with a more uniform collective response.

In Fig. 3, we compare the performance of the metasurface when illuminated using different light sources: a broadband supercontinuum laser (*i.e.,* a coherent source with strong collimation), and a tungsten-halogen lamp. The comparison between these measurements indicates that the Q increases with the coherence of the light source — using the thermal light source reduces the Q-factor by a factor of 2–5 when compared to the laser. Additionally, it decreases the resonance coupling strength, as is evident from the reduced extinction ratio of the SLRs. Figure 3b summarizes the Q-factors extracted from these measurements and compares them to numerical predictions. Note that even when using an incoherent source, the largest array still produces a very large Q-factor ($Q \sim 1000$). The observation of such a high Q using an incoherent source reinforces the validity of our aforementioned metasurface design criteria — that is, the importance of the choice of nanostructure geometry and of the array size.

The Q-factors for the type of device presented here could be further increased by considering larger arrays, or by further optimizing the nanostructure dimensions — instead of rectangles, a more intricate nanostructure shape could tailor A_0, λ_{LSPR}, and γ more independently, or could increase coupling to more neighbouring particles using out-of-plane oscillations[50]. The Q-factor could also perhaps be improved using dielectric particles; however, these materials would necessitate much larger particle sizes in order to match the scattering strength of plasmonic nanostructures. Additionally, dielectric materials possess smaller optical nonlinearities, which is undesirable for nonlinear optical applications. Finally, the metasurface shown here can be combined with other established methods to enable multiple simultaneous resonances in order to fully tailor the transmission spectrum of a wavelength-scale surface[26,51,57].

Before concluding, we take a moment to place our results in the appropriate context. To the best of our knowledge, our work represents the first experimental demonstration of an ultra-high-Q metasurface nanoresonator in any material platform, presenting an order-of-magnitude improvement over even low-loss dielectric implementations (see Sec. S4: Literature survey). Here, we would like to emphasize that this assessment does not include waveguide-coupled devices such as whispering gallery mode resonators, microring resonators or photonic crystals, where Q routinely exceeds 10^6 [18,58–60]. However, contrary to these other devices, a metasurface can easily be accessed by a beam propagating in free space, and operates entirely within a sub-wavelength propagation region. Therefore, a plasmonic high-Q metasurface enables an alternative series of specialized optical responses, including phase-matching-free nonlinear optical effects, strong localized field-enhancements, multi-mode operation, and a spatially localized optical response. Additionally, our device follows simple design principles that can be easily expanded upon, making this platform notably flexible when compared to, for instance, photonic crystals[61].

To summarize, we have fabricated and experimentally demonstrated a plasmonic metasurface nanoresonator with an unprecedentedly high Q-factor which is in excellent agreement with numerical predictions. We have found that the observed Q-factor obtained from an SLR may be limited by a poor choice of nanostructure dimensions, a small array size, or poor spatial coherence of the source illumination; we hypothesize that one or many of these factors, and not necessarily the material absorption or fabrication imperfections as has been hypothesized by others, may have been the cause for the low Q-factors reported in previous experiments featuring SLRs. This result highlights the potential of SLR-based metasurfaces, and dramatically expands the capabilities of the ultra-thin metasurface platform for many optical applications.

References

1. Saleh, B. E. A. & Teich, M. C. *Fundamentals of Photonics* (Wiley, 2007).
2. Yariv, A. & Yeh, P. *Photonics: Optical Electronics in Modern Communications* (Oxford University Press, New York, 2007), sixth edn.
3. Little, B. E., Chu, S. T., Haus, H. A., Foresi, J. & Laine, J. P. Microring resonator channel dropping filters. *Journal of Lightwave Technology* **15**, 998–1005 (1997).
4. Heebner, J., Wong, V., Schweinsberg, A., Boyd, R. & Jackson, D. Optical transmission characteristics of fiber ring resonators. *IEEE Journal of Quantum Electronics* **40**, 726–730 (2004).

5. Siegman, A. E. *Lasers* (University Science Books, Sausalito, CA, 1986), revised edn.

6. Kovach, A. *et al.* Emerging material systems for integrated optical Kerr frequency combs. *Advances in Optics and Photonics* **12**, 135–222 (2020).

7. Smith, P. W. & Turner, E. H. A bistable Fabry-Perot resonator. *Applied Physics Letter* **30**, 280 (1977).

8. Heebner, J. E. & Boyd, R. W. Enhanced all-optical switching by use of a nonlinear fiber ring resonator. *Applied Physics Letter* **24**, 847 (1999).

9. Choi, D.-Y. *et al.* Imaging-based molecular barcoding with pixelated dielectric metasurfaces. *Science* **360**, 1105–1109 (2018).

10. Vollmer, F. & Arnold, S. Whispering-gallery-mode biosensing: Label-free detection down to single molecules. *Nature Methods* **5**, 591–596 (2008).

11. Boyd, R. W. & Heebner, J. E. Sensitive disk resonator photonic biosensor. *Applied Optics* **40**, 5742–5747 (2001).

12. Sun, Y. & Fan, X. Optical ring resonators for biochemical and chemical sensing. *Analytical and Bioanalytical Chemistry* **399**, 205–211 (2011).

13. Yesilkoy, F. *et al.* Ultrasensitive hyperspectral imaging and biodetection enabled by dielectric metasurfaces. *Nature Photonics* **13**, 390–396 (2019).

14. Boyd, R. W. *Nonlinear Optics* (Elsevier, 2008).

15. Serpengzel, A., Griffel, G. & Arnold, S. Excitation of resonances of microspheres on an optical fiber. *Optics Letters* **20**, 654 (1995).

16. Armani, D. K., Kippenberg, T. J., Spillane, S. M. & Vahala, K. J. Ultra-high-Q toroid microcavity on a chip. *Nature* **421**, 925–928 (2003).

17. Akahane, Y., Asano, T., Song, B. S. & Noda, S. High-Q photonic nanocavity in a two-dimensional photonic crystal. *Nature* **425**, 944–947 (2003).

18. Zhang, X., Choi, H. S. & Armani, A. M. Ultimate quality factor of silica microtoroid resonant cavities. *Applied Physics Letters* **96**, 153304 (2010).

19. Meinzer, N., Barnes, W. L. & Hooper, I. R. Plasmonic meta-atoms and metasurfaces. *Nature Photonics* **8**, 889–898 (2014).

20. Hakala, T. K. *et al.* Lasing in dark and bright modes of a finite-sized plasmonic lattice. *Nature Communications* **8**, 13687 (2017).

21. Yang, A. *et al.* Real-time tunable lasing from plasmonic nanocavity arrays. *Nature Communications* **6**, 6939 (2015).

22. Liu, S. *et al.* An all-dielectric metasurface as a broadband optical frequency mixer. *Nature Communications* **9**, 2507 (2018).

23. Michaeli, L., Keren-Zur, S., Avayu, O., Suchowski, H. & Ellenbogen, T. Nonlinear surface lattice resonance in plasmonic nanoparticle arrays. *Physical Review Letters* **118**, 243904 (2017).

24. Huttunen, M. J., Rasekh, P., Boyd, R. W. & Dolgaleva, K. Using surface lattice resonances to engineer nonlinear optical processes in metal nanoparticle arrays. *Physical Review A* **97**, 053817 (2018).

25. Czaplicki, R. *et al.* Less Is More: Enhancement of second-harmonic generation from metasurfaces by reduced nanoparticle density. *Nano Letters* **18**, 7709–7714 (2018).

26. Huttunen, M. J., Reshef, O., Stolt, T., Dolgaleva, K. & Boyd, R. W. Efficient nonlinear metasurfaces by using multiresonant high-Q plasmonic arrays. *Journal of the Optical Society of America B* **36**, 118 (2019).

27. Chen, S., Reineke, B., Li, G., Zentgraf, T. & Zhang, S. Strong Nonlinear Optical Activity Induced by Lattice Surface Modes on Plasmonic Metasurface. *Nano Letters* **19**, 6278–6283 (2019).

28. Luo, L. *et al.* Broadband terahertz generation from metamaterials. *Nature communications* **5**, 3055 (2014).

29. Kwiat, P. G. *et al.* New High-Intensity Source of Polarization-Entangled Photon Pairs. *Physical Review Letters* **75**, 4337–4341 (1995).

30. Michler, P. *et al.* A quantum dot single-photon turnstile device. *Science* **290**, 2282–2285 (2000).

31. Yang, Y., Kravchenko, I. I., Briggs, D. P. & Valentine, J. All-dielectric metasurface analogue of electromagnetically induced transparency. *Nature Communications* **5**, 5753 (2014).

32. Thackray, B. D. *et al.* Super-narrow, extremely high quality collective plasmon resonances at telecom wavelengths and their application in a hybrid graphene-plasmonic modulator. *Nano Letters* **15**, 3519–3523 (2015).

33. Campione, S. *et al.* Broken Symmetry Dielectric Resonators for High Quality Factor Fano Metasurfaces. *Nano Letters* **3**, 2362–2367 (2016).

34. Le-Van, Q. *et al.* Enhanced Quality Factors of Surface Lattice Resonances in Plasmonic Arrays of Nanoparticles. *Advanced Optical Materials* **7**, 1801451 (2019).

35. Oldenburg, S. J., D., A. R., Westcott, S. L. & Halas, N. J. Nanoengineering of optical resonances. *Chemical Physics Letters* **288**, 243–247 (1998).

36. Maier, S. A. *Plasmonics: Fundamentals and Applications* (2007).

37. Kauranen, M. & Zayats, A. V. Nonlinear plasmonics. *Nature Photonics* **6**, 737 (2012).

38. Novotny, L. & Van Hulst, N. Antennas for light. *Nature Photonics* **5**, 83–90 (2011).

39. Wang, D., Guan, J., Hu, J., Bourgeois, M. R. & Odom, T. W. Manipulating Light, ÄìMatter Interactions in Plasmonic Nanoparticle Lattices. *Accounts of Chemical Research* **52**, 2997–3007 (2019).

40. Butet, J., Brevet, P.-F. & Martin, O. J. F. Optical second harmonic generation in plasmonic nanostructures: from fundamental principles to advanced applications. *ACS Nano* **9**, 10545–10562 (2015).

41. Auguié, B. & Barnes, W. L. Collective resonances in gold nanoparticle arrays. *Physical Review Letters* **101**, 143902 (2008).

42. Kravets, V. G., Kabashin, A. V., Barnes, W. L. & Grigorenko, A. N. Plasmonic surface lattice resonances: A review of properties and applications. *Chemical Reviews* **118**, 5912–5951 (2018).

43. Khlopin, D. *et al.* Lattice modes and plasmonic linewidth engineering in gold and aluminum nanoparticle arrays. *Journal of the Optical Society of America B* **34**, 691 (2017).

44. Rodriguez, S. R. *et al.* Coupling Bright and Dark Plasmonic Lattice Resonances. *Physical Review X* **1**, 021019 (2011).

45. Zou, S., Janel, N. & Schatz, G. C. Silver nanoparticle array structures that produce remarkable narrow plasmon line shapes. *Journal of Chemical Physics* **120**, 10871–10875 (2004).

46. Humphrey, A. D., Meinzer, N., Starkey, T. A. & Barnes, W. L. Surface lattice resonances in plasmonic arrays of asymmetric disc dimers. *ACS Photonics* **3**, 634–639 (2016).

47. Zakomirnyi, V. I. *et al.* Refractory titanium nitride two-dimensional structures with extremely narrow surface lattice resonances at telecommunication wavelengths. *Applied Physics Letters* **111**, 123107 (2017).

48. Danilov, A. *et al.* Ultra-narrow surface lattice resonances in plasmonic metamaterial arrays for biosensing applications. *Biosensors and Bioelectronics* **104**, 102–112 (2018).

49. Zou, S. & Schatz, G. C. Theoretical studies of plasmon resonances in one-dimensional nanoparticle chains: Narrow lineshapes with tunable widths. *Nanotechnology* **17**, 2813–2820 (2006).

50. Huttunen, M. J., Dolgaleva, K., Törmä, P. & Boyd, R. W. Ultra-strong polarization dependence of surface lattice resonances with out-of-plane plasmon oscillations. *Optics Express* **24**, 28279–28289 (2016).

51. Reshef, O. *et al.* Multiresonant High-Q Plasmonic Metasurfaces. *Nano Letters* **19**, 6429–6434 (2019).

52. Markel, V. A. Divergence of dipole sums and the nature of non-Lorentzian exponentially narrow resonances in one-dimensional periodic arrays of nanospheres. *Journal of Physics B: Atomic, Molecular and Optical Physics* **38**, L115–, ÄìL121 (2005).

53. Knight, M. W. *et al.* Aluminum plasmonic nanoantennas. *Nano Letters* **12**, 16000–6004 (2012).

54. McKinnon, W. R. *et al.* Extracting coupling and loss coefficients from a ring resonator. *Optics Express* **17**, 17010 (2009).

55. Rodriguez, S. R. K., Schaafsma, M. C., Berrier, A. & Gomez Rivas, J. Collective resonances in plasmonic crystals: Size matters. *Physica B: Condensed Matter* **407**, 4081–4085 (2012).

56. Zundel, L. & Manjavacas, A. Finite-size effects on periodic arrays of nanostructures. *A. Journal of Physics: Photonics* **1**, 015004 (2019).

57. Baur, S., Sanders, S. & Manjavacas, A. Hybridization of lattice resonances. *ACS Nano* **12**, 1618–1629 (2018).

58. Ji, X. *et al.* Ultra-low-loss on-chip resonators with sub-milliwatt parametric oscillation threshold. *Optica* **4**, 619–624 (2017).

59. Asano, T., Ochi, Y., Takahashi, Y., Kishimoto, K. & Noda, S. Photonic crystal nanocavity with a Q factor exceeding eleven million. *Optics Express* **25**, 1769 (2017).

60. Hsu, C. W. *et al.* Observation of trapped light within the radiation continuum. *Nature* **499**, 188–191 (2013).

61. Genetically designed L3 photonic crystal nanocavities with measured quality factor exceeding one million. *Applied Physics Letters* **104**, 241101 (2014).

62. Palik, E. D. *Handbook of optical constants of solids* (Academic Press, Orlando, Florida, 1985).

63. Johnson, P. & Christy, R. Optical constants of the noble metals. *Physical Review B* **6**, 4370–4379 (1972).

64. Oldenburg, S. J., D., A. R., Westcott, S. L. & Halas, N. J. Discrete-Dipole Approximation For Scattering Calculations. *Journal of Optical Society of America A* **11**, 1491,Äì1499 (1994).

65. Jensen, T., Kelly, L., Lazarides, A. & Schatz, G. C. Electrodynamics of Noble Metal Nanoparticles and Nanoparticle Clusters. *Journal of Cluster Science* **10**, 295–317 (1999).

66. Jackson, J. D. *Classical Electrodynamics* (John Wiley & Sons, Inc., Hoboken, NJ, USA, 1999), third edn.

67. Schulz, S. A. *et al.* Quantifying the impact of proximity error correction on plasmonic metasurfaces [Invited]. *Optical Material Express* **5**, 2798,Äì2803 (2015).

68. Chu, Y., Schonbrun, E., Yang, T. & Crozier, K. B. Experimental observation of narrow surface plasmon resonances in gold nanoparticle arrays. *Applied Physics Letters* **93**, 81108 (2008).

69. Kravets, V. G., Schedin, F., Kabashin, A. V. & Grigorenko, A. N. Sensitivity of collective plasmon modes of gold nanoresonators to local environment. *Optics Letters* **35**, 956–958 (2010).

70. Yang, A. *et al.* Real-time tunable lasing from plasmonic nanocavity arrays. *Nature Communications* **6**, 6939 (2015).

71. Li, S. Q. *et al.* Ultra-sharp plasmonic resonances from monopole optical nanoantenna phased arrays. *Applied Physics Letters* **104**, 231101 (2014).

72. Singh, R. *et al.* Ultrasensitive terahertz sensing with high-Q Fano resonances in metasurfaces. *Applied Physics Letters* **105**, 171101 (2011).

73. Wu, C. *et al.* Fano-resonant asymmetric metamaterials for ultrasensitive spectroscopy and identification of molecular monolayers. *Nature Materials* **11**, 69–75 (2011).

74. Koshelev, K. *et al.* Subwavelength dielectric resonators for nonlinear nanophotonics. *Science* **367**, 288–292 (2020).

Acknowledgements Fabrication in this work was performed in part at the Centre for Research in Photonics at the University of Ottawa (CRPuO). The authors acknowledge support from the Canada Excellence Research Chairs (CERC) Program, the Canada Research Chairs (CRC) Program, and the Natural Sciences and Engineering Research Council of Canada (NSERC) Discovery funding program. MSBA acknowledges the support of the Ontario Graduate Scholarship (OGS), the University of Ottawa Excellence Scholarship, and the University of Ottawa International Experience Scholarship. OR acknowledges the support of the Banting Postdoctoral Fellowship of the NSERC. YM was supported by the Mitacs Globalink Research Award. MJH acknowledges the support of the Academy of Finland (Grant No. 308596) and the Flagship of Photonics Research and Innovation (PREIN) funded by the Academy of Finland (Grant No. 320165).

Author Contributions MSBA, OR, and MJH conceived the basic idea for this work. OR and MSBA performed the FDTD simulations. MJH, MSBA and OR performed the lattice sum calculations. OR and GC fabricated the device. MZA and MJH designed the preliminary experimental setup. MSBA and YM carried out the measurements. OR, MSBA, and YM analysed the experimental results. JU, BS, JMM, MJH, RWB, and KD supervised the research and the development of the manuscript. MSBA and OR wrote the first draft of the manuscript. All co-authors subsequently took part in the revision process and approved the final copy of the manuscript. Portions of this work were presented at the 2020 SPIE Photonics West conference in San Francisco, CA.

Data and code availability The data that support the plots within this paper, the code used to analyze the data, the related simulation files, and other findings of this study are available from the corresponding authors upon reasonable request.

Methods

Simulations

FDTD: Full-wave simulations were performed using a commercial three-dimensional finite-difference time-domain (3D-FDTD) solver. A single unit cell was simulated using periodic boundary conditions in the in-plane dimensions and perfectly matched layers in the out-of-plane dimension. The structures were modelled using fully dispersive optical material properties for silica[62] and for gold[63]. Minimal artificial absorption ($\mathrm{Im}(n) \sim 10^{-4}$) was added to the background medium to reduce numerical divergences.

LSA: The lattice sum approach (LSA) is a variant of the discrete-dipole approximation (DDA) method[64]. It is a semi-analytic calculation method that has been found to produce accurate results for plasmonic arrays[24,26,50–52]. The main assumption in LSA when compared to DDA is that of an infinite array of identical dipoles[50]. It has the capability to model finite-sized arrays with an arbitrary number of nanostructures. Its rapid simulation time makes it a good tool for iterating many simulations to study trends and behaviours of entire metasurfaces, especially for finite array effects.

Using the LSA approach, the dipole moment $\vec{p}$ of any particle in the array is written as

$$\vec{p} = \frac{\varepsilon_0 \alpha(\omega) \vec{E}_{\mathrm{inc}}}{1 - \varepsilon_0 \alpha(\omega) \mathcal{S}(\omega)} \equiv \varepsilon_0 \alpha^*(\omega) \vec{E}_{\mathrm{inc}}, \tag{3}$$

where the effect of inter-particle coupling is incorporated in the lattice sum $\mathcal{S}$, and α^* is the effective polarizability. This equation produces Eq. (2) in the main text. The calculations presented in this work also incorporate a modified long-wavelength correction[65]:

$$\alpha(\omega) \rightarrow \frac{\alpha(\omega)}{1 - \frac{2}{3} i k^3 \alpha(\omega) - \frac{k^2}{l} \alpha(\omega)}, \tag{4}$$

where k is the wavenumber in the background medium $k = (2\pi n/\lambda)$ and l is the effective particle radius. Also here, minimal artificial absorption ($\mathrm{Im}(n) = 6 \times 10^{-4}$) was added to the refractive index $n = 1.452$ of the background medium to reduce numerical divergences associated with the approach when considering large arrays[52]. We set $l = 180$ nm for all calculations. For a planar array of N dipoles, the lattice sum term $\mathcal{S}$ is

$$\mathcal{S}(\omega) = \sum_{j=1}^{N} \frac{\exp(\mathrm{i} k r_j)}{\varepsilon_0 r_j} \left[k^2 + \frac{(1 - \mathrm{i} k r_j)(3\cos^2\theta_j - 1)}{r_j^2} \right], \tag{5}$$

where r_j is the distance to the j^{th} dipole, and θ_j is the angle between $\vec{r}_j$ and the dipole moment $\vec{p}$.

The optical transmission spectra can be obtained by using the optical theorem, $\mathrm{Ext} \propto k\mathrm{Im}(\alpha^*)$[66]:

$$T(\omega) = 1 - \frac{4\pi k}{P_x P_y} \mathrm{Im}[\alpha^*(\omega)], \tag{6}$$

where P_x and P_y are the lattice constants along the x and y dimensions, respectively.

To produce the plots in Figs. 1a – c, we performed an LSA calculation using the following parameters for the single dipole: $\lambda_{\mathrm{LSPR}} = 830$ nm; $A_0 = 2.98 \times 10^{-7}$ m^3/s, $\gamma = 1/[2\pi(2.1\text{ fs})] \approx 7.6 \times 10^{13}$ s^{-1}. LSA parameters were determined by matching to FDTD data. The lattice constants were $P_x = 500$ nm and $P_y = 1060$ nm. The total array size was 600×600 μm^2, corresponding to $N_x = 1200 \times N_y = 567$ nanostructures, respectively. The LSA calculations in Fig. 3 used these same parameters, but varied the total number of nanostructures.

To calculate the figures in Fig. 2a – c, we performed a series of LSA calculation using the following parameters for the particle: $A_0 = 3.98 \times 10^{-7}$ m^3/s, $\gamma = 1/[2\pi(2.1\text{ fs})] \approx 7.6 \times 10^{13}$ s^{-1}. The dipole resonance wavelengths λ_{LSPR} were 800, 833, 866, 900, 933, 966 and 1000 nm, respectively. The lattice constants were $P_x = 500$ nm and $P_y = 1060$ nm, respectively. The total array size was 600×600 μm^2, corresponding to $N_x = 1200 \times N_y = 567$ nanostructures, respectively. To obtain Fig. 2d, a series of LSA calculations were performed for many values of λ_{LSPR} ranging from 800 nm to 1000 nm, and the Q-factors were extracted from the results using a fit to a Lorentzian. The curves in **(d)** come from repeating this procedure with oscillator strengths of $A_0 = 3.98 \times 10^{-7}$, 4.38×10^{-7} and 4.77×10^{-7} m^3/s.

Device details

We fabricated different metasurface devices with array sizes of 300×300 μm^2, 400×400 μm^2, 500×500 μm^2, and 600×600 μm^2, with a corresponding number of participating nanostructures of 600×284, 800×378, 1000×472, and 1200×567, respectively. The lattice constants of the rectangular arrays are $P_x = 500$ nm $\times$ $P_y = 1060$ nm. The dimensions of the rectangular gold nanostructures are $L_x = 130$ nm $\times$ $L_y = 200$ nm, with a thickness of $t = 20$ nm. The lattice is embedded within a homogeneous background $n \approx 1.46$.

Fabrication

The metasurfaces are fabricated using a standard metal lift-off process. We start with a fused silica substrate. We deposit a silica undercladding layer using sputtering. We then define the pattern using electron-beam lithography in a positive tone resist bi-layer with the help of a commercial conductive polymer. The mask was designed using shape-correction proximity error correction[67] to correct for corner rounding. Following development, a thin adhesion layer of chromium (0.2 nm thick) is deposited using e-beam evaporation, followed by a layer of gold deposited using thermal evaporation. Lift-off is performed, and a final protective silica cladding layer is deposited using sputtering. The initial and final silica layers are sputtered using the same tool under the same conditions to ensure that the environment surrounding the metasurface is completely homogeneous. Before characterization, the surface of the device is then covered in index-matching oil. The backside of the silica substrate is coated with an anti-reflective coating to minimize substrate-related etalon fringes.

Characterization

See Sec. S5: Experimental setup for a schematic of the experimental setup.

Coherent light measurements: To measure the transmission spectra, we flood-illuminated all of the arrays in the sample using a collimated light beam from a broadband supercontinuum laser source. The wavelength spectrum of the source ranges from $\lambda = 470$ to 2400 nm. The beam comes from normal incidence along the z-direction with light polarized in the x-direction. The incident polarization is controlled using a broadband linear polarizing filter. Light transmitted by the metasurface is then imaged by a $f = 35$ mm lens, and a 100 μm pinhole is placed in the image plane to select the desired array. The transmitted light is collected in a large core (400 μm) multimode fiber and analyzed using an optical spectrum analyzer, and is normalized to a background trace of the substrate without gold nanostructures. The resolution of the spectrometer is set to 0.01 nm.

Incoherent light measurements: Here, the experiment goes as above, but the samples are excited using a collimated tungsten-halogen light source (ranging from $\lambda = 300$ to 2600 nm) and a 400 μm pinhole.

Supplementary Information

Below is the supplementary information for *Ultra-high-Q resonances in plasmonic metasurfaces* by M. Saad Bin-Alam, Orad Reshef, Yaryna Mamchur, M. Zahirul Alam, Graham Carlow, Jeremy Upham, Brian T. Sullivan, Jean-Michel Ménard, Mikko J. Huttunen, Robert W. Boyd, and Ksenia Dolgaleva. Section S1 shows the dependence of the SLR behaviour on the particle geometry, produced using FDTD simulations. In Sec. S2, we present supporting material for Fig. 2d. In Sec. S3, we present a representative image of a fabricated device. In Sec. S4, we present a literature survey for experimentally reported high-Q metasurfaces. In Sec. S5, we describe our experimental setup.

S1 Dependence of SLR behaviour on particle dimensions

To explicitly demonstrate how changing the dimensions of the nanoparticle may affect the properties of the SLR, we perform full-wave simulations in FDTD using a series of particle geometries. Figure S1 depicts the simulation results. Not only the Q-factor, but also λ_{SLR} and the extinction ratio are all affected by changes in the particle dimensions.

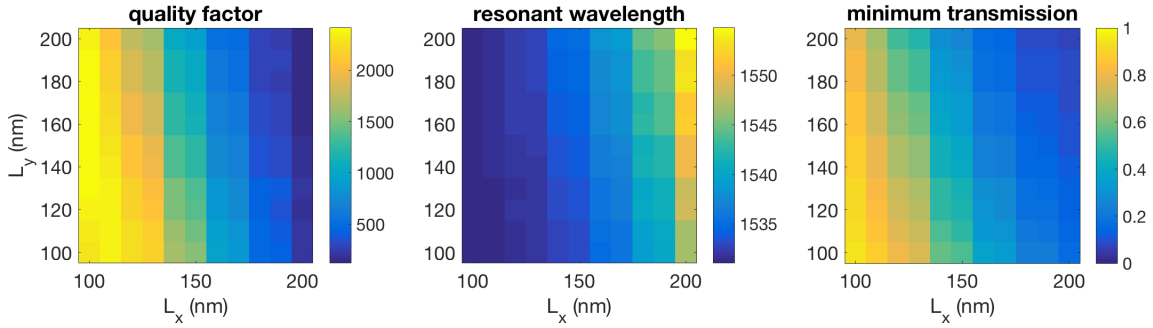

Fig. S1 | Particle dimension sweep. Quality factor Q (left), resonant wavelength λ_{SLR} (center), and minimum transmission as a function of particle dimensions L_x and L_y, extracted from full-wave simulations performed with FDTD.

S2 Q-factor extraction

Figure S2 shows Lorentzian fits (red curves) to a series of LSA calculations (black curves) with varying λ_{LSPR} (see Methods for values). The Q-factors extracted from these fits are used to produce the black curves in Fig. 2d. In Fig. S3, we reproduce the fits to the measurements that produced the values for Fig. 3b.

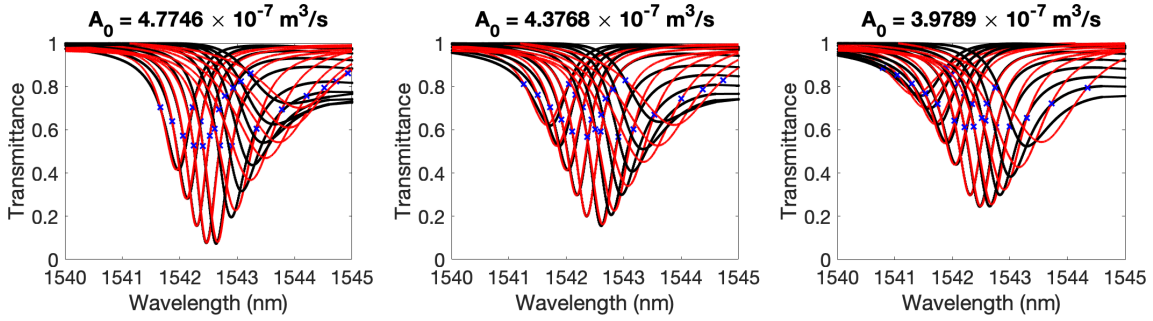

Fig. S2

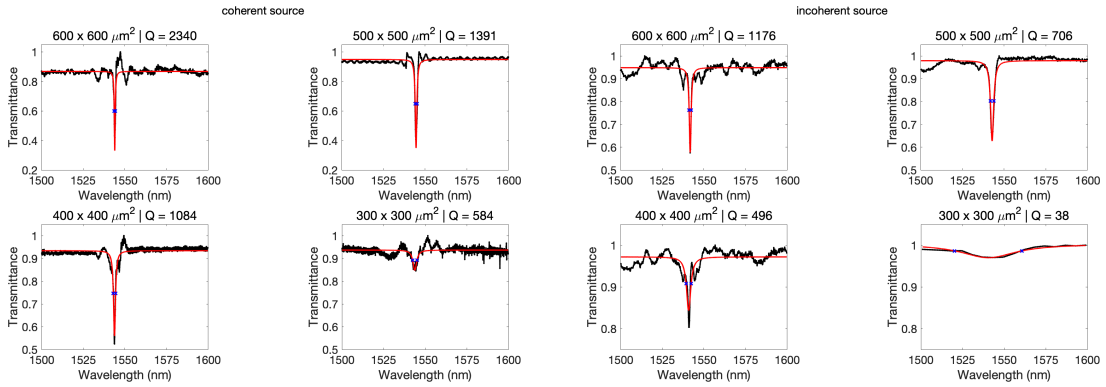

Fig. S3

S3 Image of the device

Figure S4 shows a typical optical image for one of the devices taken with a bright field microscope. Surrounding the device are large aluminum alignment marks to help locate the device in the experimental setup.

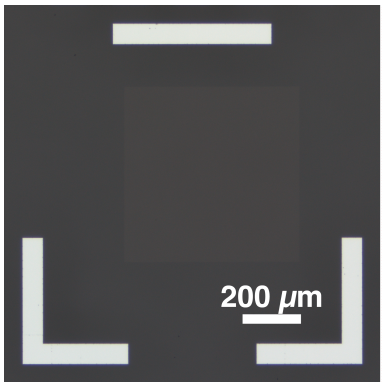

Fig. S4 | Optical image of a 600×600 μm^2 array.

S4 Literature survey

Table 1 contains a short survey of the literature on metasurface nanocavities. Other than the reported Q-factors, we have included, when available, information that is relevant to compare their work against ours, such as the operating wavelength, the material platform, the array size and the type of light source used.

Mechanism	Q	λ (nm)	Material	Light source	Array size (μm^2)	Reference
SLR	**2400**	**1550**	**Au NPs**	**Supercontinuum**	**600×600**	**This work**
LSPR	<10	700	Au NPs	Tungs.-Halogen lamp	3000×3000	[44]
SLR	25	930	Au NPs	Collimated source	135×135	[68]
SLR	30	850	Au NPs	Tungs.-Halogen lamp	3000×3000	[44]
SLR	60	800	Au NPs	Tungs.-Halogen lamp	35×35	[41]
SLR	150	764	Au NPs	Tungs.-Halogen lamp	N/A	[69]
SLR	230	900	Au NPs	Laser	$\sim 10000 \times 10000$	[70]
SLR	300	1500	Au nanostripes	Tungs.-Halogen lamp	300×100	[32]
SLR	330	648	Ag NPs	Tungs.-Halogen lamp	2500×2500	[34]
Mirror Image	200	5000	ITO nanorods	Collimated source	N/A	[71]
EIT	483	1380	Si	Tungs.-Halogen lamp	225×240	[31]
Fano Resonance	65	THz	Al Particles	THz laser	10000×10000	[72]
Fano Resonance	100	THz	Au Assym. NPs	FTIR	150×150	[73]
Fano Resonance	350	1000	Si	N/A	N/A	[33]
Fano Resonance	600	1000	GaAs	N/A	N/A	[33]
BIC	200	930	AlGaAs	Laser	N/A	[74]

Table 1. Summary of experimentally obtained Q-factors in metasurfaces. Q, quality-factor; λ, resonance wavelength; NP, nanoparticle; SLR, surface lattice resonance; LSPR, localized surface plasmon resonance; EIT, Electromagnetically induced transparency

S5 Experimental setup

A broadband source is collimated and is polarized using a broadband linear polarizing filter. A first iris is optionally placed to help align the sample in the center of the beam. The beam is then passed through the sample. The surface of the device is imaged using an $f = 35$ mm lens, and a pinhole is placed in the image plane to select the desired array. The transmitted light is collected in a large core (400 µm diameter) multimode fiber and is analyzed using an optical spectrum analyzer.

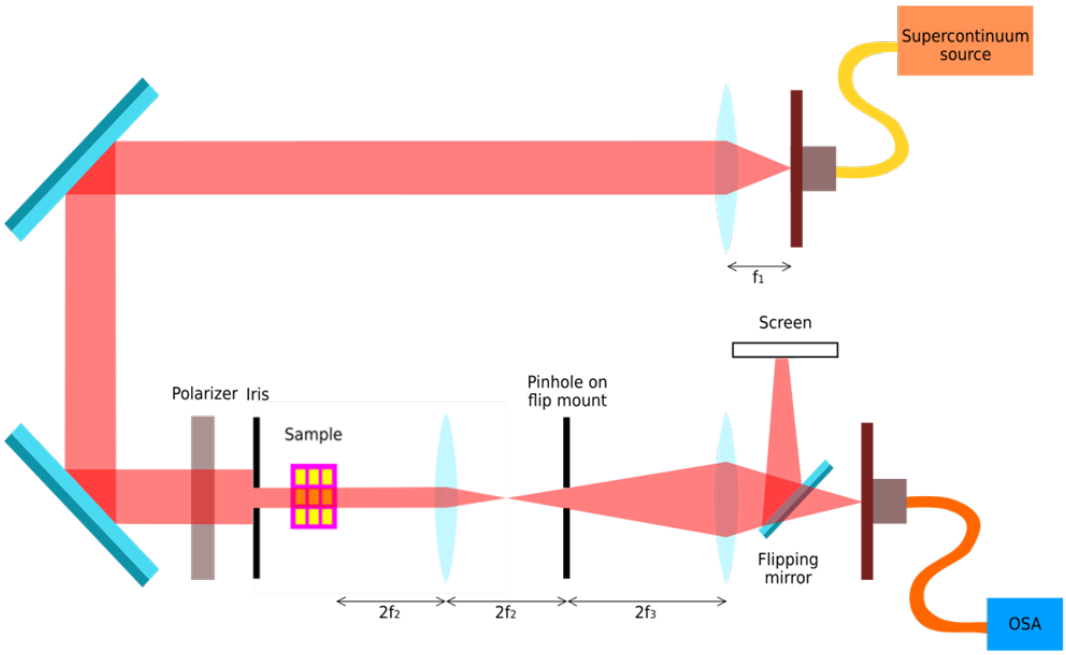

Fig. S5 | Experimental setup.